



UNIVERSIDADE ESTADUAL DE CAMPINAS
SISTEMA DE BIBLIOTECAS DA UNICAMP
REPOSITÓRIO DA PRODUÇÃO CIENTÍFICA E INTELLECTUAL DA UNICAMP

Versão do arquivo anexado / Version of attached file:

Versão do Editor / Published Version

Mais informações no site da editora / Further information on publisher's website:

<https://www.sciencedirect.com/science/article/pii/S0264127518305483>

DOI: 10.1016/j.matdes.2018.07.018

Direitos autorais / Publisher's copyright statement:

©2018 by Elsevier. All rights reserved.

DIRETORIA DE TRATAMENTO DA INFORMAÇÃO

Cidade Universitária Zeferino Vaz Barão Geraldo

CEP 13083-970 – Campinas SP

Fone: (19) 3521-6493

<http://www.repositorio.unicamp.br>



Meta-equilibrium transition microstructure for maximum austenite stability and minimum hardness in a Ti-stabilized supermartensitic stainless steel☆

J.D. Escobar^{a,*}, J.P. Oliveira^b, C.A.F. Salvador^a, G.A. Faria^c, J.D. Poplawsky^d, J. Rodriguez^e, P.R. Mei^a, S.S. Babu^{f,g}, A.J. Ramirez^c

^a College of Mechanical Engineering, University of Campinas – FEM - Unicamp, Campinas, SP 13083-860, Brazil

^b UNIDEMI, Department of Mechanical and Industrial Engineering, NOVA School of Science and Technology, NOVA University Lisbon, 2829-516 Caparica, Portugal

^c Welding Engineering, Department of Materials Science and Engineering, The Ohio State University, 1248 Arthur E. Adams Drive, Columbus, OH 43221, USA

^d The Center for Nanophase Materials Sciences, Oak Ridge National Laboratory, 37831, USA

^e Mechanical Engineering Department, EIA University, Envigado, Colombia

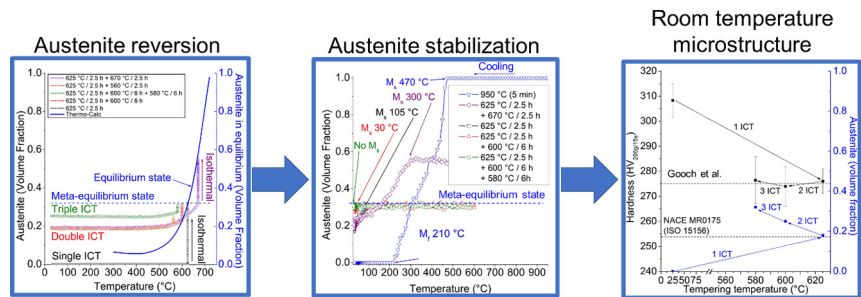
^f Mechanical, Aerospace and Biomedical Engineering, University of Tennessee, Knoxville, TN 37996-2210, USA

^g Manufacturing Demonstration Facility, Oak Ridge National Laboratory, Knoxville, TN, USA

HIGHLIGHTS

- Compositional gradients after single tempering forced a meta-equilibrium during the second and third tempering cycles.
- Nucleation at the Ni-poor tempered matrix was suppressed.
- Site-specific austenite reversion occurred at the Ni-rich fresh martensite laths.
- The softening mechanism was insensitive to the maximization of austenite after double and triple tempering.

GRAPHICAL ABSTRACT



ARTICLE INFO

Article history:

Received 28 May 2018

Received in revised form 8 July 2018

Accepted 9 July 2018

Available online 20 July 2018

ABSTRACT

The maximization of stable reverted austenite at room temperature through inter-critical tempering is a widely used method to reduce hardness in supermartensitic stainless steels. Nevertheless, partial martensitic transformation might occur due to insufficient compositional stabilization. In this work, we conducted a time-resolved triple-step inter-critical tempering, specially designed to obtain maximum austenite stability and minimum hardness through the progressive suppression of the martensitic transformation. The mechanism behind the progressive increase in stable reverted austenite was the generation of a meta-equilibrium state, which imposed a

Abbreviations: α_{eq} , ferrite in thermodynamic equilibrium; α'_f , fresh martensite; α'_t , tempered martensite; γ , used to generically refer to austenite; γ_{eq} , austenite in thermodynamic equilibrium; γ_r , reverted austenite stabilized at room temperature; APT, Atom Probe Tomography; EDS, Energy Dispersive X-ray Spectroscopy; ICT, inter-critical tempering; SMSS, supermartensitic stainless steels; SXRD, synchrotron X-ray diffraction.

☆ This manuscript has been authored by UT-Battelle, LLC under Contract No. DE-AC05-00OR22725 with the U.S. Department of Energy. The United States Government retains and the publisher, by accepting the article for publication, acknowledges that the United States Government retains a non-exclusive, paid-up, irrevocable, world-wide license to publish or reproduce the published form of this manuscript, or allow others to do so, for United States Government purposes. The Department of Energy will provide public access to these results of federally sponsored research in accordance with the DOE Public Access Plan (<http://energy.gov/downloads/doe-public-access-plan>).

* Corresponding author.

E-mail addresses: juliandescobar@gmail.com, jdescoba01@fem.unicamp.br (J.D. Escobar), jp.oliveira@campus.fct.unl.pt (J.P. Oliveira), csalvador@fem.unicamp.br (C.A.F. Salvador), abrefaria.1@buckeyemail.osu.edu (G.A. Faria), poplawskyjd@ornl.gov (J.D. Poplawsky), johnnatan.rodriguez@eia.edu (J. Rodriguez), pmei@fem.unicamp.br (P.R. Mei), sbabu@utk.edu (S.S. Babu), ramirezlondono.1@osu.edu (A.J. Ramirez).

Keywords:

Atom Probe Tomography
Austenite reversion
Isothermal tempering treatments
Synchrotron diffraction

limit in both high temperature austenite reversion and room temperature austenite stabilization. Such limit corresponded to the high temperature volume fraction of austenite, obtained right before cooling from the first cycle. This effect was associated to the Ni-rich fresh martensite laths acting as local Ni compositional pockets, providing site-specific austenite reversion; and to the suppression of any additional nucleation at the Ni-poor matrix as the T₀ temperature for austenite reversion was strongly increased. The softening mechanism was mainly controlled by the carbon arrest effect by the precipitation of Ti (C, N), which was completed after the first tempering cycle. Nevertheless, maximizing reverted austenite and suppressing fresh martensite at room temperature did not result in additional hardness reductions.

© 2018 Elsevier Ltd. All rights reserved.

1. Introduction

The isothermal reversion of nano-sized austenite (γ_r) in tempered martensitic matrixes (α'_T) has regained interest in the past decade as a methodology for the design, control and optimization of the mechanical properties of martensitic steels [1–4]. As an example, the austenite reversion has been used for tailoring the mechanical properties of supermartensitic stainless steels (SMSS) pipelines in the oil and gas industry [5–9]. The maximization of the γ_r volume fraction at room temperature after inter-critical tempering (ICT) has been directly associated with the simultaneous maximization of the impact toughness and minimization of hardness [6,9–11]. The latter is especially important in order to satisfy the maximum hardness requirement of 253 HV for field applications in sour service, commonly adopted by the oil and gas industry [12]. Nevertheless, this has proven to be challenging due to the relatively small changes in hardness after tempering cycles [13,14]. Thus, a variety of methodologies for hardness minimization have been proposed, such as the reduction of C and N from the nominal composition [13] and the addition of stabilizing elements such as Ti, Nb and V to arrest the interstitial elements from the solid solution [15].

Additionally, complex multiple ICT cycles have been performed as an effort to increase the volume fraction of stable γ_r at room temperature, from 0.05 to 0.2 after single ICT cycles [16–19] up to 0.4 [6,10,20]. The increased reversion efficiency obtained by the use of multiple ICT cycles has been related to a wide variety of microstructural effects, such as the presence of retained austenite [4,16,21,22], reverted austenite and fresh martensite after a single ICT cycle [10,16,23], the precipitation of carbides [11,24] and even to compositional segregations after the controlled dissolution of carbides [2,25]. Interpreting the austenite reversion mechanism through multiple tempering cycles can be rather complex due to the aforementioned competitive microstructural effects. However, most of these can be avoided or isolated under controlled conditions in Ti-stabilized SMSS.

This work aims to clarify the kinetic and compositional aspects behind the austenite nucleation and stabilization mechanisms throughout the execution of a triple ICT cycle, designed to achieve maximum austenite stability and minimum hardness. Before tempering, samples were fully austenitized to provide a well-known starting microstructure, consisting of compositionally homogeneous fresh martensite and stable titanium carbo-nitrides, Ti (C, N), in the absence of retained austenite. Then, the samples were subjected to controlled single, double and triple ICT cycles. The evolution of the microstructure was studied by time-resolved synchrotron X-ray diffraction throughout the thermo-mechanical simulation of the multiple ICT heat treatment. Furthermore, samples were extracted after each step of the triple ICT heat-treatment in order to be further characterized using Scanning Electron Microscopy (SEM), Energy Dispersive X-Ray Spectroscopy (EDS) in Scanning Transmission Electron Microscopy (STEM) and Atom Probe Tomography (APT). The maximization of γ_r and the carbon arrest from the solid solution were directly related to the resultant hardness modifications. Results were interpreted with the aid of equilibrium and kinetic calculations.

2. Experimental

2.1. Time-resolved synchrotron X-ray diffraction during thermo-mechanical simulation

A commercial hot rolled and homogenized Ti-Stabilized SMSS with a nominal composition shown in Table 1 was used. Dog-bone type samples with 2 mm thick, 5 mm wide and 20 mm long reduced section were machined and then homogenized at 950 °C during 20 min, followed by furnace cooling to room temperature. A constant flux of Argon was used to protect the samples from decarburization and oxidation. A fully martensitic microstructure was obtained [17].

Time-resolved synchrotron X-ray diffraction (SXRD) experiments were conducted in order to study the austenite transformation kinetics during the heating, isothermal and cooling stages throughout the multiple ICT heat treatment. This analysis was performed at the X-ray scattering and thermo-mechanical simulation experimental station (XTMS), at the Brazilian National Synchrotron Source (LNLS). Incident beam energy of 12 keV was used. A thermo-mechanical simulator (Gleeble® 3S50) coupled to the synchrotron light source was used to perform the heat treatments. The first, second and third ICT cycles were conducted at 625 °C during 2.5 h, 600 °C during 6 h, and 580 °C during 6 h, respectively. A final austenitization cycle was conducted at 950 °C for 5 min, followed by cooling to room temperature. All tempering cycles were performed using the direct resistive heating method, controlled by type K thermocouples welded to the center of the reduced section of the samples. The typical temperature uncertainty was ± 1 °C. In all cases, heating and cooling rates were fixed to 0.166 °C·s⁻¹ and 5 °C·s⁻¹, respectively. The transformation temperatures at the surface and bulk of the samples were indirectly measured by X-ray diffraction and laser dilatometry data analysis, respectively. A graphical representation of the aforementioned four heat treatment cycles is shown in Fig. 1.

The quantification of the X-ray diffraction data was performed for the austenite using Eq. (1) [26,27], which establishes a relationship between the measured peak areas and the corresponding phase fractions. In this equation, F_p is the fraction of phase p, n_p is the number of peaks from phase p, K represents a given $\{hkl\}$ family, I_{pK} is the area under a peak of the family K on phase p and R_{pK} is a dimensionless scalar containing the effects of the form factor and multiplicity of each $\{hkl\}$ family for each phase, as well as the influence of the lattice parameters. Such quantification is relative to the surface since the experiment was set for X-ray reflection configuration obtained at 12 keV. The time-resolved austenite quantification was conducted using $\{111\}\gamma$, $\{200\}\gamma$ peaks and $\{110\}\alpha'$ peak. Also, a wider spectra, including $\{111\}\gamma$,

Table 1
Nominal composition of a Ti-stabilized SMSS.

	C	N	Si	Mn	Ni	Cr	Mo	Cu	Ti	V
wt%	0.024	0.0129	0.260	0.480	5.90	12.02	1.93	0.09	0.130	0.040
at.%	0.111	0.0513	0.516	0.487	5.60	12.88	1.13	0.08	0.153	0.044

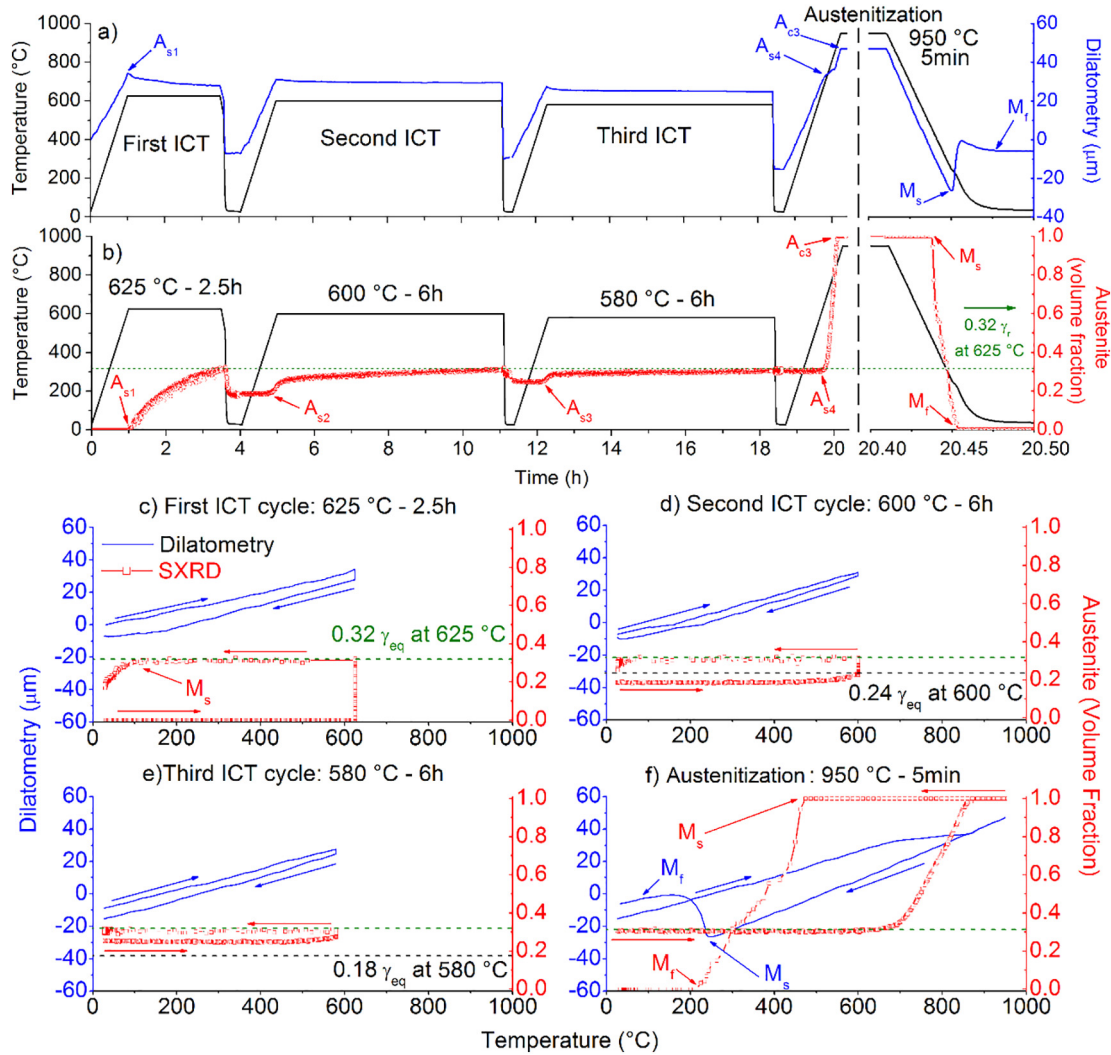


Fig. 1. Austenite reversion kinetics and austenite thermal stability measured by correlative a) laser dilatometry and b) synchrotron X-ray diffraction during a triple ICT and a final austenitization cycle. Temperature-resolved transformation kinetics during: c) first ICT cycle at 625 °C during 2.5 h; d) second ICT cycle at 600 °C during 6 h, e) third ICT cycle at 580 °C during 6 h, and f) final austenitization cycle at 950 °C during 5 min. Green and black dashed lines: Equilibrium γ volume fraction at the reversion temperatures. The experimental error for SXR data ranges between 0.005 and 0.015 vol fraction.

{200} γ , {220} γ , {311} γ , {222} γ peaks, and {110} α' , {200} α' , {211} α' , {220} α' peaks, was used for a more accurate quantification right before cooling and at room temperature after each heat treatment step.

$$F_p = \frac{\frac{1}{n_p} \sum_K \frac{I_{pK}}{R_{pK}}}{\sum_p \frac{1}{n_p} \sum_K \frac{I_{pK}}{R_{pK}}} \quad (1)$$

On the other hand, qualitative laser dilatometry was used in order to determine the inflection points at which volumetric austenite reversion (contraction) and martensitic transformation (expansion) occurred. Error bars are not included in the figures, since the uncertainty on the measured volume fractions of austenite ranged between 0.005 and 0.015 [26].

2.2. Microstructural and compositional characterization

Energy Dispersive X-ray Spectroscopy measurements were performed in Scanning Transmission Electron Microscopy (STEM-EDS) using a 200 kV FEI Tecnai F20 Microscope. Site-specific focused ion

beam (FIB) lift-outs were taken from regions with a high density of γ_t/α'_t interfaces. Thin foils were attached to Cu grids and milled to approximately 100 nm thicknesses. The compositional measurements were obtained for areas of approximately $2.2 \times 1.8 \mu\text{m}$. The spatial resolution for a camera length of 115 mm corresponded to 9 nm per pixel. Additionally, 1-D point-to-point compositional analysis was performed through several interfaces with a spatial resolution of 1 nm per point.

Atom Probe Tomography was used to find the compositional gradients across the γ_t/α'_t interfaces. Site-specific FIB lift-outs were taken from regions with a high density of γ_t/α'_t interfaces. Regions of interest were annularly milled (30 kV) and cleaned with a 2 kV ion beam to make needle-shaped specimens suitable for field evaporation. The analyses were performed using a CAMECA Instruments LEAP® 4000× HR local electrode atom probe. The specimens were field evaporated in laser mode with a 200 kHz pulse repetition rate, 30 K specimen temperature, 100 pJ laser power, and a 0.5–1.0% detection rate. The resulting data was reconstructed and analyzed using the CAMECA IVAS software. Deconvolution of the ions within overlapping isobars of different elements (e.g., Cr₅₄/Fe₅₄) was performed based on the natural abundances of the elements. Error bars for the compositional profiles were calculated according to Eq. (2), where s is the standard error assuming a

random solid solution, c_i is the atomic concentration of a solute, and n_t is the total number of ions collected [28]:

$$s = \sqrt{\frac{c_i(1-c_i)}{n_t}}, \quad (2)$$

Microhardness measurements were conducted in a LECO M-400-H1 microhardness Vickers tester. All samples were cut to expose the simulated isothermal 2 mm × 5 mm reduced cross sections right below the spot welded thermocouples. An average of twenty indents per condition were performed using a 200 g load, 200 μm step size and 15 s dwell time. Prior testing, all samples were grinded and polished down to 1 μm diamond particle size.

2.3. Thermodynamic calculations

Thermo-Calc® software and TCFE9 database were used to perform composition and volumetric phase fraction predictions. The calculations were performed for a thermodynamic system allowing the precipitation of all possible phases concerning the nominal composition of the SMSS. Gibbs free energy of α and γ were calculated also for the nominal composition as a function of the Ni concentration. Ferrite was assumed to be equivalent to martensite in terms of equilibrium volume fractions and compositions [17,21,29].

Kinetic calculations were performed using DICTRA® to simulate the austenite growth in a non-homogeneous matrix. The simulation was set up in a planar geometry with a fully implicit scheme. The grid was created with 100 points with a point distribution geometrically biased towards zero and widths of 200 nm, which corresponded to half of the average distance between clusters of reverted intra-granular austenite laths. The compositions of the phases introduced to the simulations are shown in Table 2. The model was run at 600 °C for up to 6 h (21,600 s). Phase information and elemental mobility values were retrieved from TCFE9 and MOBFE3 databases.

3. Results

3.1. Kinetic aspects of the multiple-step ICT cycle

Fig. 1 a) and b) show the time-resolved evolution of the martensite to austenite, and austenite to martensite transformation kinetics, measured by laser dilatometry (blue) and synchrotron X-ray diffraction (red), respectively. Fig. 1 c) to f) shows the detailed transformation kinetics and dilatometry for each of the three ICT cycles and the final complete austenitization step as a function of temperature. The phase transformations during the multiple ICT cycles are described as follows:

3.1.1. First ICT cycle at 625 °C during 2.5 h

The initial microstructure consisted of a fully martensitic matrix (α') with the presence of Ti (C, N). During the heating stage to 625 °C no γ reversion was detected according to SXRDX and dilatometry measurements. The $\alpha'_f \rightarrow \gamma$ transformation started within the first minute after reaching the isothermal stage. As depicted in Fig. 1 c), the isothermal reversion asymptotically evolved to 0.32 γ , which matched the predicted equilibrium volume fraction of γ_{eq} at 625 °C (green dashed line). On cooling, partial $\gamma \rightarrow \alpha'_f$ transformation started at the surface

at 105 °C, accompanied by a small change in slope due to volumetric expansion near room temperature.

3.1.2. Second ICT cycle at 600 °C during 6 h

The second ICT cycle, detailed in Fig. 1 d), started with a microstructure composed of 0.18, 0.14 and 0.68 volumetric fractions of γ_r , α'_f and α'_t , respectively. During the heating stage, γ reversion was evidenced at 523 °C (A_{s2}) by SXRDX. However, no noticeable contraction was detected by dilatometry. The isothermal transformation evolved slowly at the surface and at the bulk when compared to the first ICT cycle. The γ volume fraction grew asymptotically towards 0.32 γ , which was above the equilibrium volume fraction of γ at 600 °C (0.23 γ_{eq}). On cooling, slight $\gamma \rightarrow \alpha'_f$ transformation occurred around room temperature, both at the surface and at the bulk.

3.1.3. Third ICT cycle at 580 °C during 6 h

The third ICT cycle, detailed in Fig. 1 e), started with 0.25, 0.07 and 0.68 volumetric fractions of γ_r , α'_f and α'_t , respectively. The γ reversion on heating was observed at 547 °C (A_{s3}), with no noticeable volumetric contraction. During the isothermal stage, the transformation evolved asymptotically to 0.32 γ , which was also above the equilibrium volume fraction of γ at 580 °C (0.18 γ_{eq}). No $\gamma \rightarrow \alpha'_f$ transformation was detected upon cooling. The final room temperature microstructure was composed of 0.32 γ_r and 0.68 tempered α'_t , which matches the high-temperature equilibrium microstructure at 625 °C. Further details on the microstructural evolution will be presented in Section 4, altogether with the STEM and APT results.

3.1.4. Complete austenitization cycle at 950 °C

A final cycle of complete austenitization, depicted in Fig. 1 f), was conducted to study the thermal stability of the final microstructure after the complete suppression of $\gamma \rightarrow \alpha'_f$ transformation. The γ reversion on heating was detected at 655 (A_{s4}) at the surface by SXRDX and at 675 °C at the bulk. A fully austenitic microstructure was obtained above 870 °C (A_{c3}). Complete $\gamma \rightarrow \alpha'_f$ transformation was achieved upon cooling, both at the surface and at the bulk of the sample, due to the compositional solubilization effect inside γ at 950 °C. The M_s at the surface was 475 °C, whereas the volumetric expansion was detected at 250 °C. The transformations at the surface and bulk ended at 210 and 160 °C, respectively. The differences in the transformation temperatures, detected by the two techniques, are associated to the accelerated martensitic transformation at the surface when compared to the bulk [22, 26, 30] due to lack of constraints. The equilibrium austenite and ferrite volume fractions and compositions are presented in Table 3.

3.2. Microstructural aspects of the multiple-step ICT cycle

3.2.1. Evolution of the microstructure and morphology

Fig. 2 shows the microstructure before tempering (a), and after the first (b), second (c) and third (d) ICT cycles. The typical low-carbon lath martensite microstructure observed in the homogenized condition evolved to a microstructure composed of a high density of acicular and globular interfaces. The observed lath/matrix interfaces were produced isothermally during the first ICT cycle at 625 °C and corresponded to reverted austenite laths at high temperature. However, the differentiation between γ_r and α'_f cannot be readily made by SEM analysis due to their morphological similarities [20,31,32].

By comparing the SEM microstructures after the first, second and third ICT cycles, a very slight increase in the lath width was noticed. The previous austenite grain boundaries (PAGB) remained constant with an approximate value of 20 μm before tempering and after each of the three ICT cycles. This is expected as the austenite reversion is occurring at the lath/lath martensite interfaces and due to the Ti (C, N) grain growth pinning effect [15,33]. Based on STEM image analysis performed for all visible laths, the average lath width after the first, second and third ICT cycles were 161 ± 46 , 192 ± 63 and 195 ± 49 nm

Table 2
Phase compositions used for the kinetic simulations [17].

Phases	Cr	Mo	Ni	Mn	Fe
Ni-rich FCC	12.8	0.96	10.2	0.8	Bal.
Ni-poor FCC	12.8	0.96	8.1	0.8	Bal.
Ni-rich BCC	12.8	0.96	8.1	0.8	Bal.
Ni-poor BCC	12.8	1.2	3.1	0.35	Bal.

Table 3

Austenite and ferrite equilibrium volume fractions and compositions at the ICT temperatures.

°C	Vol. fraction	Composition (at.%)									
		Fe	Cr	Mn	Mo	Ni	Si	Ti	C	N	
Austenite in equilibrium											
625	0.32	Bal.	11.7	1.2	0.7	10.6	0.6	5E−3	2.1E−3	9.1E−10	
600	0.24	Bal.	11.4	1.6	0.7	12.8	0.7	5E−3	1.0E−3	2.9E−10	
580	0.18	Bal.	11.1	2.0	0.7	14.7	0.7	6E−3	0.5E−3	1.1E−10	
Ferrite in equilibrium											
625	0.68	Bal.	12.8	0.2	0.7	3.2	0.5	8E−3	0.1E−3	3E−10	
600	0.76	Bal.	12.6	0.2	0.6	3.5	0.5	7E−3	4.7E−5	3E−10	
580	0.82	Bal.	12.5	0.2	0.6	3.7	0.5	7E−3	2.5E−5	3E−10	

respectively. Whereas, the spacing between laths corresponded to 431 ± 98 , 354 ± 69 and 376 ± 92 nm, respectively. The high deviation in size and spacing can be associated with inhomogeneous shapes and to the coalescence of laths due to γ/α'_t interface motion throughout the second and third ICT cycles.

3.2.2. Compositional evolution

Fig. 2 e) to m) shows the elemental maps obtained via STEM-EDS after the first (e, h, k), second (f, i, l) and third (g, j, m) ICT cycles. Fig. 2 e), f) and g), presents the distribution of Ni (green), Mo (red) and Ti (blue), respectively and Fig. 2 h), i) and j), shows the distribution of Cr (magenta) and Si, respectively. Additionally, 1-D STEM-EDS compositional analysis was performed for Cr, Ni, Mo, Ti and Si along adjacent reverted laths indicated by white arrows in Fig. 2 k), l) and m). Results are presented in Fig. 3 a), b) and c) for the first, second and third ICT cycles, respectively.

From Fig. 2, it was evidenced that the strong partitioning of Ni (green) into the reverted laths was the main factor involved in the austenite stabilization mechanism. No evidence of partitioning of α -stabilizer elements, such as Cr, Mo, Ti and Si was observed by STEM-EDS. However, these elements were found at the Ti (C, N) and χ precipitates, identified as local clusters of Ti (white arrows), and Cr + Si + Mo (yellow arrows), respectively.

Quantitative area distribution of Ni between the reverted laths and the α'_t matrix is presented in Fig. 2 k), l) and m), after single, double and triple ICT cycles, respectively. Hot colors represent high local concentrations of Ni, cold colors represent depletion of Ni. Results showed an evident non-homogeneous distribution of this element. This was observed both within the reverted laths and along the α'_t matrix.

After a single ICT cycle, the average area distribution of Ni inside the reverted laths (Fig. 2 k)) ranged between 10 and 12.5 at.% Ni. The 1-D characterization depicted in Fig. 3 a) showed an overall tendency to match the local equilibrium Ni partitioning expected at 625 °C (dashed green lines in Fig. 3). Local 1-D absolute minimum and maximum values of 8.4 and 14.5 at.% Ni were observed within the reverted laths. However, due to the relatively high scattering of the compositional data, all profiles were softened by a 5-point average method. Raw (spots) and averaged (lines) profiles are shown together. For the averaged case, a more representative behavior was obtained, where the minimum and maximum values within the laths after 1 ICT were 9.2 and 13% at.

Regarding the area distribution of Ni along the α'_t matrix (Fig. 2 k)), Ni-depleted areas below 2.5 at.% were observed, especially at regions in-between adjacent reverted laths. Whereas, other regions with Ni concentrations above 5 at.% were evidenced away from clusters of laths. The 1-D characterization analysis (Fig. 3 a)) showed minimum and maximum averaged values of 2.5 and 4 at.%. Regions with low density of laths showed Ni concentrations near or slightly above the local equilibrium for α (dotted green line in Fig. 3).

After double (Fig. 2 l)) and triple (Fig. 2 m)) ICT cycles, an overall Ni enrichment of the reverted laths was observed. This was directly associated to the increment in the γ_f volume fraction from Fig. 1 d) and e). The

1-D compositional characterization evidenced maximum averaged Ni concentrations of 14 at.% (Fig. 3 b)) and 13.2 at.% (Fig. 3 c)). The pixels with high local concentrations of Ni observed by area analysis were related to the local peaks observed by 1-D compositional analysis. Maximum non-averaged values of 15.8 and 14.2% of Ni, were measured after double and triple ICT cycles, respectively.

On the other hand, the α'_t matrix evidenced further Ni depletion in areas between laths, especially after the triple ICT cycle. In this case, the presence of regions with average Ni concentrations between 2.5 and 5 at.% was reduced. Whereas, more regions with Ni concentration below 2.5 at.% appeared (Fig. 2 m)). After double and triple ICT cycles, the 1-D compositional analysis evidenced stable averaged minimum Ni concentrations of 2.5 at.%, which were below the local equilibrium for α for all the tempering temperatures (Table 3).

Although multiple tempering cycles increased the volume fraction of stable γ_f , such complex heat treatment also led to the preferential precipitation of χ at the reverted lath/matrix interfaces, as depicted in Figs. 2 f), g) and 3 c). The characterization of χ using APT compositional analysis is presented in Fig. 4 a) and in Table 4.

Negligible partitioning of Cr, Mo, Si and Ti between the reverted laths and the α'_t matrix can be assumed from the 1-D compositional analysis. However APT compositional analysis across the lath/matrix interfaces confirmed strong interface segregation of Cr and Mo. The distribution of the most representative alloying elements is presented in Fig. 4 a) and c) after triple ICT. The Ti and C clustering indicated the presence of Ti (C, N); whereas, the Mo and Ti clustering indicated the presence of χ . Fig. 4 b) and d) present the 1-D compositional profile across two different lath/ α'_t interfaces, represented as red arrows. The concentration of Ni within four reverted laths ranged between 9.6 and 10.2 at.%. Whereas, Ni depletion between 2 and 2.6 at.% (below the equilibrium for α) was seen at the α'_t matrix. This is consistent with the 1-D STEM-EDS compositional analyses.

3.3. The relationship between stable reverted austenite and hardness

The evolution of the hardness for the different ICT cycles is depicted in Fig. 5. The softening effect was mostly related to the first ICT cycle, which produced a mixed microstructure composed of 0.18 γ_f and 0.14 α'_f in a tempered martensite matrix. Even after achieving maximum γ_f stability by the total suppression of α'_f in an α'_t matrix, no further hardness reduction was achieved. After triple ICT, the softest regions within the microstructure were still 20 HV above the maximum admissible hardness limit of 253 HV, suggested by corrosion standards for applications in the oil and gas industry [12–14].

4. Discussion

4.1. Microstructural evolution during multiple-stage ICT cycles

Fig. 6 summarizes the microstructural evolution of γ_f after single, double and triple ICT cycles. When the starting microstructure corresponded to a fully homogenized martensitic matrix, the $\alpha'_f \rightarrow \gamma$ kinetics evolved towards the austenite equilibrium volume fraction, relative to its reversion temperature. However, decreasing the isothermal reversion temperature resulted in slower and incomplete reversion transformations [16,26].

After the first ICT cycle at 625 °C during 2.5 h, the microstructure evolved from PAGB enclosing a typical low carbon fresh martensite microstructure in the homogenized condition [4,34], to PAGB containing a high density of acicular and globular γ_f/α'_t and α'_f/α'_t interfaces similarly to [5,11,31,35]. By the end of the isothermal transformation, a given number of lath/matrix interfaces, corresponding to 0.32 volume fraction of γ , were generated. This modified non-homogeneous microstructure imposed a new meta-equilibrium due to the generation of strong compositional gradients.

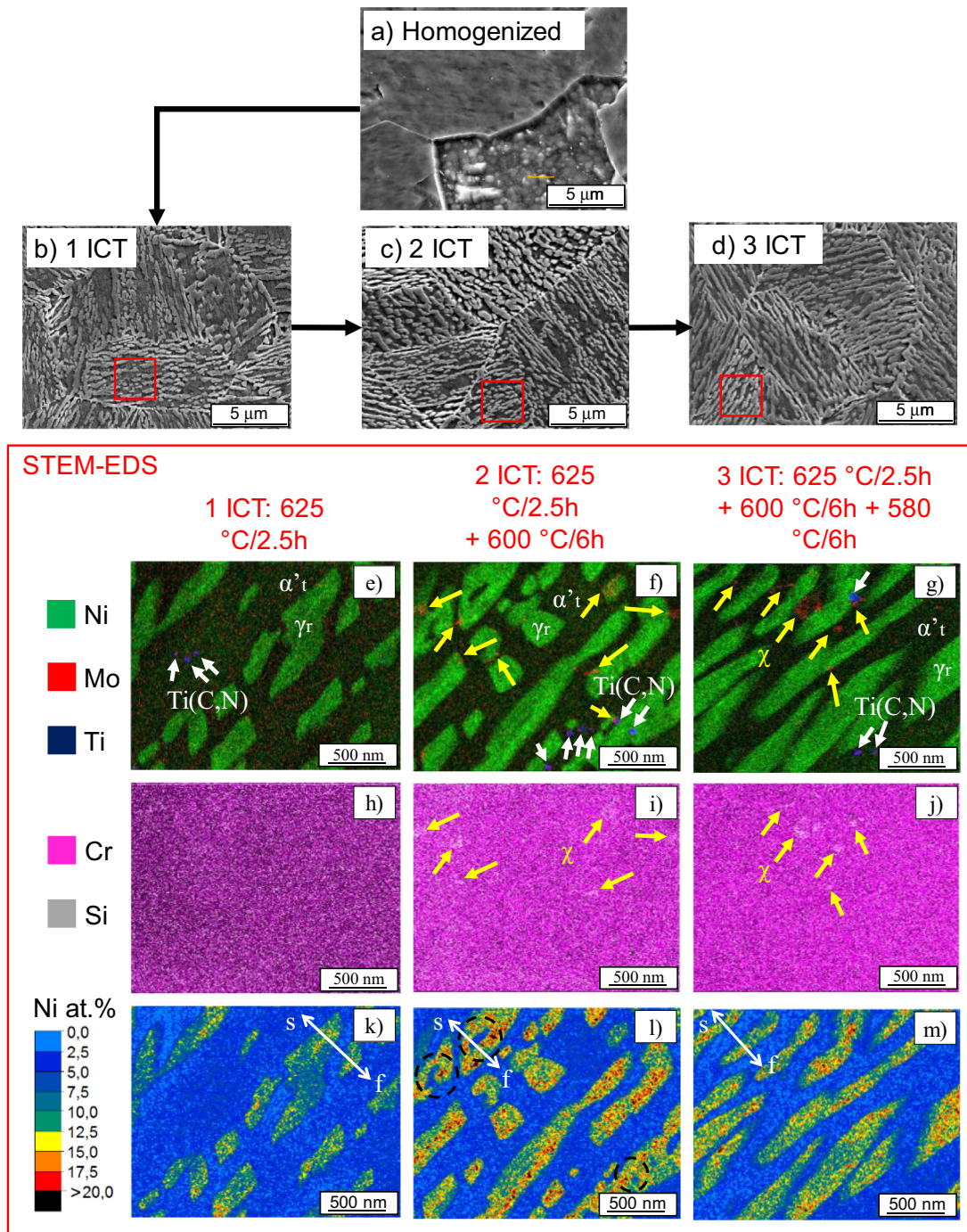


Fig. 2. SEM characterization after: a) Homogenization at 950 °C – 20 min, and subsequent ICT cycles at b) 625 °C – 2.5 h, c) 625 °C – 2.5 h + 600 °C – 6 h, and d) 625 °C – 2.5 h + 600 °C – 6 h + 580 °C – 6 h. STEM-EDS compositional characterization after single (e, h, k), double (f, i, l) and triple (g, j, m) ICT cycles. EDS qualitative Ni, Mo, Ti, Cr and Si (e–j) and quantitative Ni distribution (k–m). Yellow and white arrows indicate the presence of χ and Ti (C,N) precipitates, respectively.

All subsequent multiple ICT cycles whose isothermal temperature were below 625 °C evolved asymptotically towards the new meta-equilibrium volume fraction of 0.32 γ . Such limit was in all cases above the global equilibrium condition, which is achievable under a fully homogenized matrix [26].

On the other hand, when the second ICT cycle was conducted above 625 °C, the austenite volume fraction grew above the meta-equilibrium and reached the global equilibrium condition. This is due to the increased Ni diffusivity and to the reduced Ni partitioning between γ and α , necessary for interface motion at higher temperatures.

4.2. Compositional evolution during multiple-stage ICT cycles

Fig. 7 depicts a summary of the compositional evolution of the samples after single, double and triple ICT cycles. Overall, Ni enrichment of the reverted laths was observed. However, large standard deviations were noticed among the available laths and the isolated matrix. This was caused by the non-homogeneous distribution of Ni within both constituents. Although 1-D STEM-EDS and APT measurements allowed data collection with higher spatial and compositional resolution, these can suffer from lack of statistic

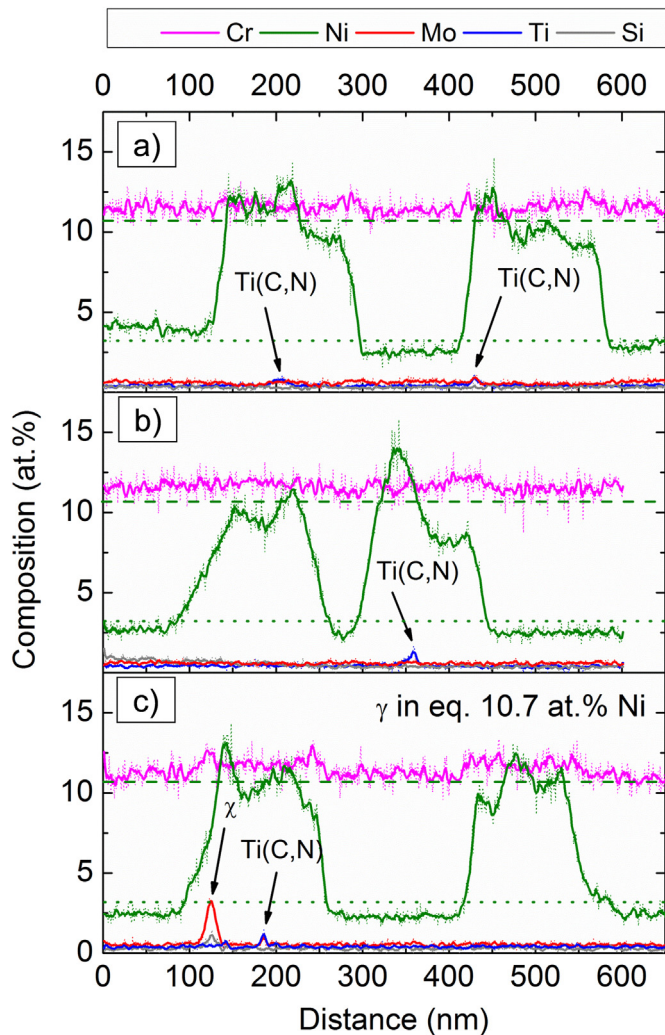


Fig. 3. 1-D STEM-EDS line-profile compositional analysis along two adjacent γ_r laths, measured after the a) first, b) second and c) third ICT cycles. The dashed and dotted lines represent the equilibrium composition for γ and α at 625 °C, respectively. The compositional profiles were softened by averaging 5 consecutive data points. The original profile is shown behind as scattered dots.

representability when compared to a more comprehensive area analysis. This was evidenced by the relatively high scattering of such compositional data. Despite the scattering, it is worth reminding that STEM-EDS and APT compositional measurements were within the standard deviation of the area measurements.

The C0-Ni composition, defined as the critical Ni concentration at which the Gibbs free energies of ferrite and austenite are the same under constant temperature and pressure, was calculated. This strategy has been used for the determination of the critical carbon content in retained austenite and bainite in carbon steels [36–39], and to interpret the diffusive to displacive transition affecting the γ reversion mechanism in SMSS [18]. As depicted in Fig. 7, a clear separation between the reverted laths and the α'_t matrix was evidenced. Throughout the multiple ICT cycles, the Ni content of the reverted laths evolved above the C0-Ni composition, preserving an FCC structure at high temperature. On the other hand, the α'_t matrix provided the additional Ni to the γ_r/α'_t interfaces, losing Ni down to a concentration that stabilized a bcc structure. Nevertheless, being above the C0-Ni composition did not guarantee complete austenite thermal stability upon cooling, as shown in Fig. 1 c) and d).

Three kinetic simulations, shown in Fig. 8, were performed in order to understand the role of Ni in the austenite stabilization mechanism for

a non-homogeneous matrix, considering: a) Ni-poor FCC lath in a Ni-poor tempered BCC matrix; b) FCC nuclei, growing epitaxially at expenses of a Ni-rich BCC lath in a Ni-poor tempered BCC matrix; and c) Ni-rich FCC lath in a Ni-poor tempered BCC matrix, aided by a Ni-rich BCC lath, separated by a typical lath distance of 400 nm. These results were directly compared to three APT measurements (i, ii and iii) of γ_r laths after triple ICT in d). The simulations were performed for a temperature of 600 °C, using database diffusivity and increasing the BCC diffusivity by a factor of 50 [21]. The latter was used to take into account the effect of the faster diffusivity of Ni in BCC due to a higher dislocation density inherent to martensite [17,21,40]. In all cases, the increased mobility accelerated the simulated transformations.

If the transformation followed the equilibrium path, a portion of the reverted austenite should have been dissolved in order to reach the global equilibrium volume fraction of γ in 600 and 580 °C. Such dissolution, best represented in Fig. 8 a), would imply lath size reductions and strong Ni build-ups at the retreating interfaces. However, this was not experimentally observed due to the formation of a meta-equilibrium microstructure with a new limit of 0.32 γ_r . In fact, the average lath widths of 161 ± 46 , 192 ± 63 and 195 ± 49 nm, measured after single, double and triple ICT, respectively, evidenced a small increment.

A second case can be considered assuming epitaxial growth of an FCC nucleus at expenses of a Ni-rich BCC lath, as presented in Fig. 8 b). The FCC/BCC interface advances aided by the flux of Ni coming from the Ni-rich BCC lath. A new FCC lath is formed with a Ni partitioning according to the tie-lines at 600 °C. The austenite reversion stops when the Ni is exhausted from the BCC regions, resulting in a net gain in the volumetric fraction of stable FCC. However, evidence of new laths with flat Ni profiles and partitioning according to the second and third ICT local equilibrium conditions was not observed.

A third hypothesis, depicted in Fig. 8 c), considers a system containing a Ni-rich FCC lath and a Ni-rich BCC lath, separated by a Ni-poor BCC matrix. The interface between the Ni-rich FCC and the Ni-poor tempered BCC matrix initially tends to retreat, and then to advance again for longer reversion times or increased BCC diffusivity. The Ni-rich BCC regions will tend to dissolve, providing a Ni flux towards the advancing interface. A new Ni-rich layer grows on top of the original Ni-rich FCC lath, and its size will be determined by the excess of Ni above the Ni in equilibrium of α at 600 °C. This was observed in cases (i) and (iii) in Fig. 8 d) and has been reported by other authors in Mn-controlled austenite reversion [4,21]. Although no experimental observation of lath dissolution was observed, it is clear that any excess of Ni in BCC will be rapidly dissolved and diffused towards the FCC/BCC interfaces. Therefore, this hypothesis seems to more accurately represent the ongoing transformation during the second and third ICT cycles.

The relatively high scattering and deviation from the expected equilibrium compositions can be associated mainly to two reasons. First, the reverted laths are compositionally inhomogeneous due to the possible coalescence of laths, mainly along the longitudinal lath direction (case ii in Fig. 8 d)). The distance between portions of reverted austenite along the same lath is smaller when compared to the typical distance between two adjacent laths. Therefore, such coalescence might result in a reverted austenite lath composed by a string of Ni-rich and Ni-poor interconnected regions. Additionally, the lack of compositional homogenization within austenite, especially at the lower portion of the inter-critical field [40], can be possible due to the slower diffusivity of Ni in FCC when compared to BCC. Niessen et al., performed a detailed analysis of 28 compositional datasets, including APT and TEM characterization of reverted austenite and tempered martensite of low carbon martensitic stainless steels. Results evidenced a high deviation of Ni in austenite of 2 wt % lower than the predicted equilibrium composition. Whereas, the Ni content in the martensite matrix evidenced a better agreement with the predicted values [41].

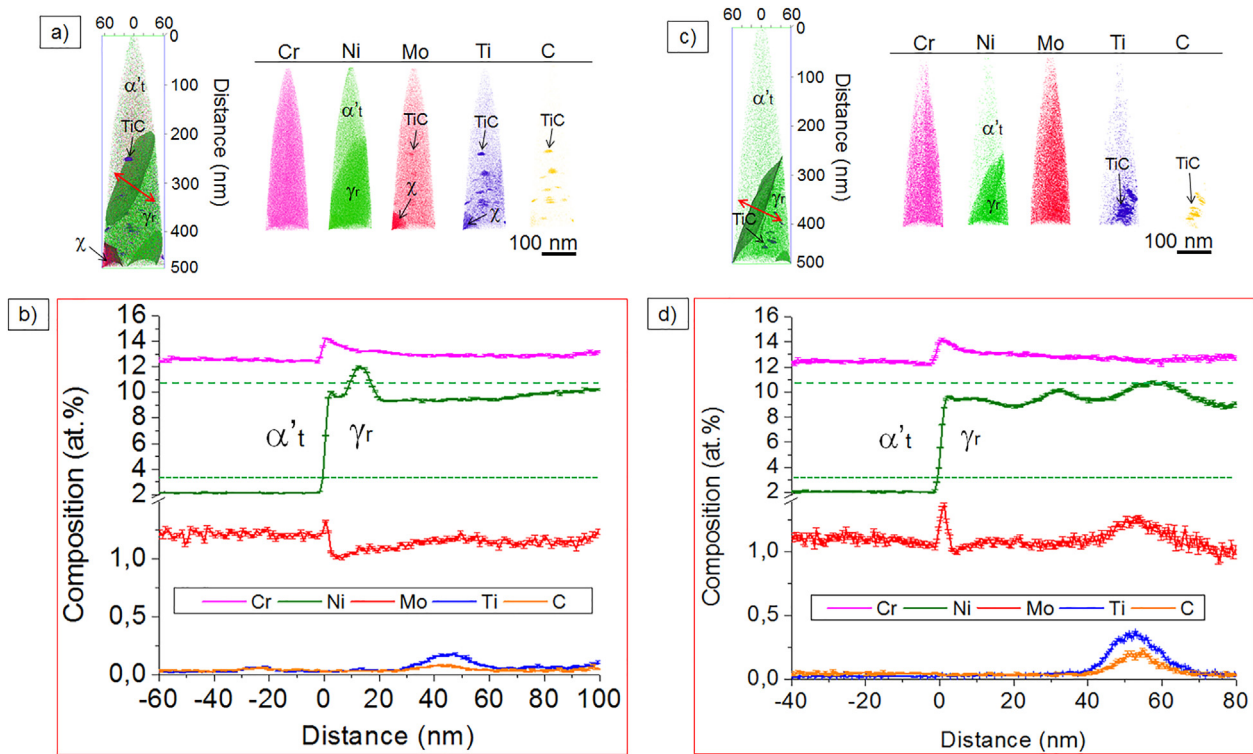


Fig. 4. APT compositional analysis of two different samples after 3 cycles of IC tempering. The Cr, Ni, Mo, Ti and C atom maps of each sample are shown in a) and d). The compositional profiles across the γ_r/α'_t interfaces for both samples are shown in b) and d). Austenite/martensite and Carbide/martensite interfaces were defined with 5 at.% Ni and 20 at.% Ti + C isoconcentration surfaces.

4.3. Changing the nucleation mechanism: homogeneous to the non-homogeneous matrix

For the interpretation of the nucleation mechanism, the T₀-Ni temperature was calculated as a function of the Ni content, which is the element controlling the transformation [17,40,41]. The Gibbs free energy curves were plotted with Ni concentrations varying between 0 and 20 at.%, based on the nominal SMSS composition, and then subtracted point-to-point for each calculated temperature to obtain the T₀ curve. The T₀-Ni temperature represents the critical temperature at which the Gibbs free energy of austenite and ferrite are equal for a given nominal Ni content. Results are shown in Fig. 9.

After tempering, the heterogeneous microstructure was divided into three compositionally differentiable constituents: stable γ_r laths (represented in yellow) evidencing Ni contents above 9.9 at.%, an α'_t matrix (represented in blue) highly depleted in Ni below 4 at.%, and fresh α'_t laths (represented in green) with Ni contents above C₀-Ni and below 9.9% at.

For a compositionally homogeneous microstructure, the nominal Ni content of 5.6 at.% (red dotted line) matched the C₀-Ni composition at 625 °C. Therefore, the $\alpha'_t \rightarrow \gamma$ reversion is expected to occur immediately after reaching the isothermal stage. This is consistent with the experimental observations in Fig. 1 a), b) and c). In this case, heterogeneous nucleation will occur at preferential sites, such as lath/lath martensite interfaces [4,11,35,42,43] and can be aided by the presence of carbides [24,25,44].

Table 4
Peak deconvolution analysis of χ precipitates after triple ICT (at.%).

	Fe	Mo	Cr	Si	Ni	Ti	C	Nb	V
Average	46.00	22.80	20.70	5.78	3.57	0.465	0.007	0.02	0.08
Error	0.04	0.03	0.03	0.02	0.01	0.006	0.001	0.00	0.00

For the Ni-depleted α'_t matrix with a Ni content between 4 and 2 at.% Ni (grey region), which is the average case for the 1-D characterization after the second and third ICT cycles, the $\alpha'_t \rightarrow \gamma$ reversion is unlikely to occur at 600 and 580 °C. Further nucleation is inhibited during the multiple ICT cycles since the T₀-Ni temperature for the Ni-depleted matrix ranges between 670 and 720 °C.

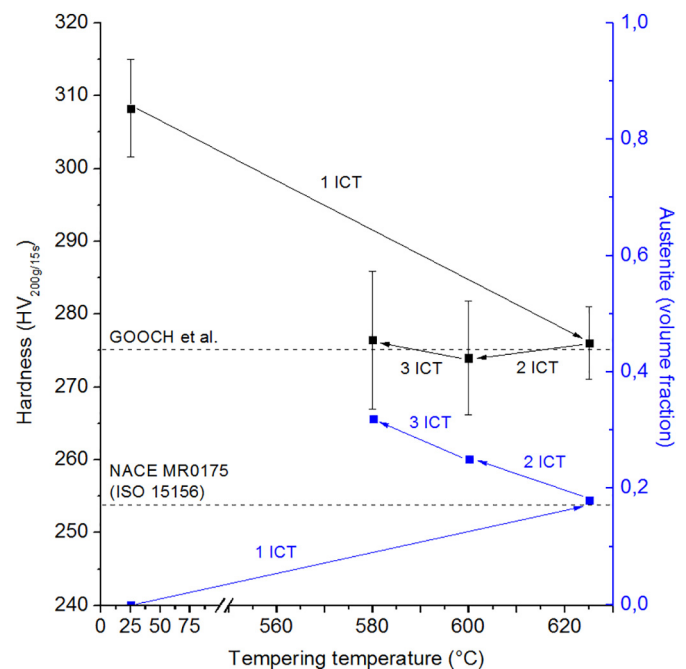


Fig. 5. The relationship between the amount of stable reverted austenite and hardness as a function of the thermal history. ICT: inter-critical tempering cycle. The experimental error for SXRD data ranges between 0.005 and 0.015 vol fraction.

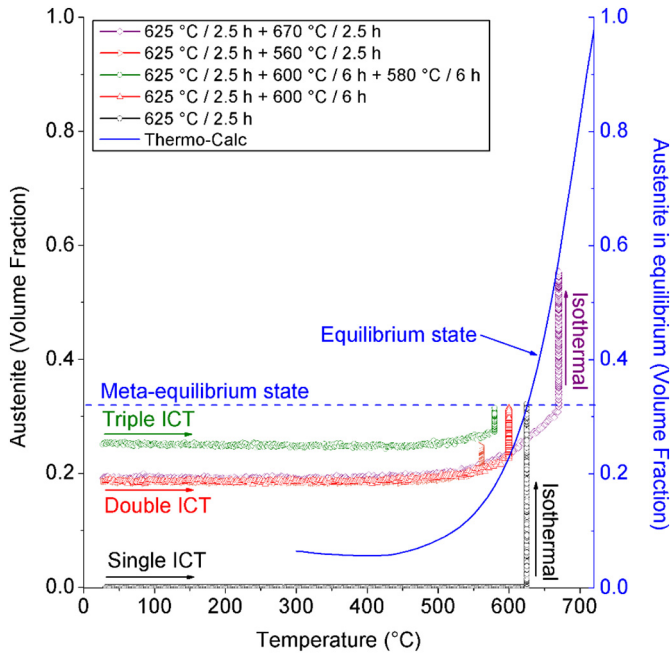


Fig. 6. Austenite reversion kinetics for a homogenized matrix (black) during single ICT, and non-homogeneous matrixes (red and green) during double and triple ICT cycles. The blue curve represents the global equilibrium state. The horizontal dashed blue line represents the meta-equilibrium state imposed by the first ICT cycle. The experimental error for SXR data ranges between 0.005 and 0.015 vol fraction.

During the second and third ICT cycles, the nucleation mechanism changed from the lath/lath fresh martensite interfaces to the preferential reversion of the Ni-rich fresh martensite laths, resulting from the

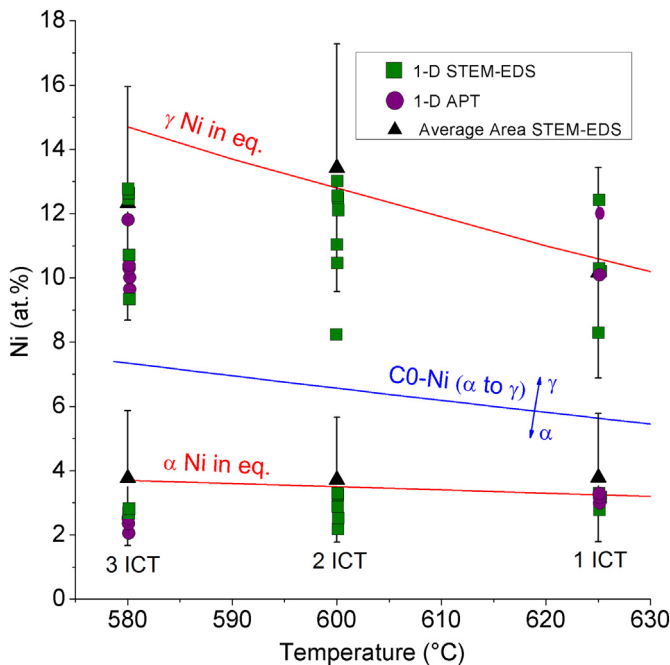


Fig. 7. Compositional evolution of the reverted laths and the tempered martensite matrix throughout the triple ICT cycle. The composition was measured by 1-D STEM-EDS (green squares), 1-D APT (violet circles), and average area measurements by STEM-EDS (black triangles + dispersion). The upper and lower red lines indicate the equilibrium composition of austenite and ferrite, respectively. The blue line (C0-Ni) indicates the critical Ni content at which Gibbs free energy of austenite and ferrite are equal and spontaneous reversion can occur.

cooling stages. This is explained by the reduction of the interface energy, since the α'_f laths already exist and can act as preferential nucleation sites for heterogeneous nucleation due to reduced nucleation energy [45,46], and by the strong compositional gradients between the reverted laths and the α'_t Ni-depleted matrix. Results from Belde et al., showed that the austenite nucleation mechanism can be modified by compositional gradients, through the vessel phase effect [2,25]. Strong but local compositional inhomogeneities left after partial dissolution of $M_{23}C_6$ carbides not only allowed the site-specific nucleation of austenite but resulted in controlled morphologies.

Therefore, after single ICT, the α'_f laths act as local Ni containers, resulting in the site-specific reversion of austenite upon multiple ICT cycles. Little or no additional lath growth was observed due to the low mobility of the interfaces, caused by the combined effect of the increased partitioning of Ni into austenite for lower IC temperatures [26,39,47] and to the little additional Ni left in a Ni-depleted α'_t matrix. Additionally, the high density of dislocations inherent to the martensitic transformation is expected to assist the reversion and stabilization process of the Ni-rich α'_f laths, acting as low-energy sites for nucleation with enhanced mobility of γ -stabilizing elements [17,21,22,40,44].

4.4. Reverted austenite thermal stability upon heating and cooling

4.4.1. Variation of the A_s temperature upon heating

The modification of the A_s temperatures as a function of the multiple ICT cycles is shown in Fig. 9. The A_{s1} , for the solubilized microstructure, corresponded to 625 °C, which matches the C0-Ni composition for 5.6 at.% of Ni. The A_{c1} measured at $0.167\text{ °C}\cdot\text{s}^{-1}$ for a homogenized composition corresponded to $625 \pm 3\text{ °C}$ [26]. When comparing the A_{s2} , A_{s3} and A_{s4} temperatures to the T0-Ni, it can be inferred that the Ni-richer α'_f laths will revert to austenite first, since the martensite with the lower Ni content presents higher A_{c1} temperatures [23,47]. The A_s temperature was progressively shifted towards higher temperatures due to the stabilization of the Ni-richer α'_f laths, and to the remaining presence of the Ni-depleted α'_f laths, which needed longer times to reach the critical Ni concentration for complete stability upon cooling.

After complete stabilization of γ_r , the austenite growth above the A_{s4} was related to several competing effects. Slightly above A_{s4} , the γ/α'_t interface motion is aided by the reduction of the equilibrium partitioning of Ni with the increasing temperature. Then, at the higher portion of the inter-critical region, the compositional homogenization effect inside the austenite laths become relevant [40], providing additional Ni towards the advancing interface. Finally, possible nucleation and growth of additional γ might occur near the A_{c3} temperature due to the drop in the C0-Ni composition aided by the dissolution of the remaining precipitates [23].

4.4.2. Variation of the M_s temperature upon cooling

Fig. 10 summarizes the $\gamma \rightarrow \alpha'_f$ transformation kinetics measured by SXR at the surface of the samples upon cooling from the first, second and third ICT isothermal stages, and from the complete austenitization cycle at 950 °C. The partial $\gamma \rightarrow \alpha'_f$ transformation upon cooling from 625 °C was associated to a possible compositional gradient of Ni between 5.6 at.% (C0-Ni-zero at 625 °C) and 9.6 at.% (A_{s2}). During the second ICT cycle, more γ laths were enriched, and thus, the M_s was dislocated to around 30 °C. In this case, the unstable $\gamma \rightarrow \alpha'_f$ transformation was related to a Ni gradient between 6.6 at.% (C0-Ni at 600 °C) and 8.5 at.% (A_{s3}). The suppression of the $\gamma \rightarrow \alpha'_f$ transformation was achieved after the triple ICT cycle. The average Ni content in γ_r , measured for 4 samples by APT, is $9.9 \pm 0.4\text{ at.}\%$. Then, the last portion of Ni-rich α'_f laths involved local Ni enrichment from 7.3 at.% (C0-Ni at 580 °C), to the final measured $9.9 \pm 0.4\text{ at.}\%$. Complete $\gamma \rightarrow \alpha'_f$ transformation upon cooling from 950 °C was observed since the concentration of Ni inside γ was homogenized to 5.6 at.%.

A series of TEM compositional measurements available in the literature have shown that, after ICT cycles in SMSS, the γ_r usually presented

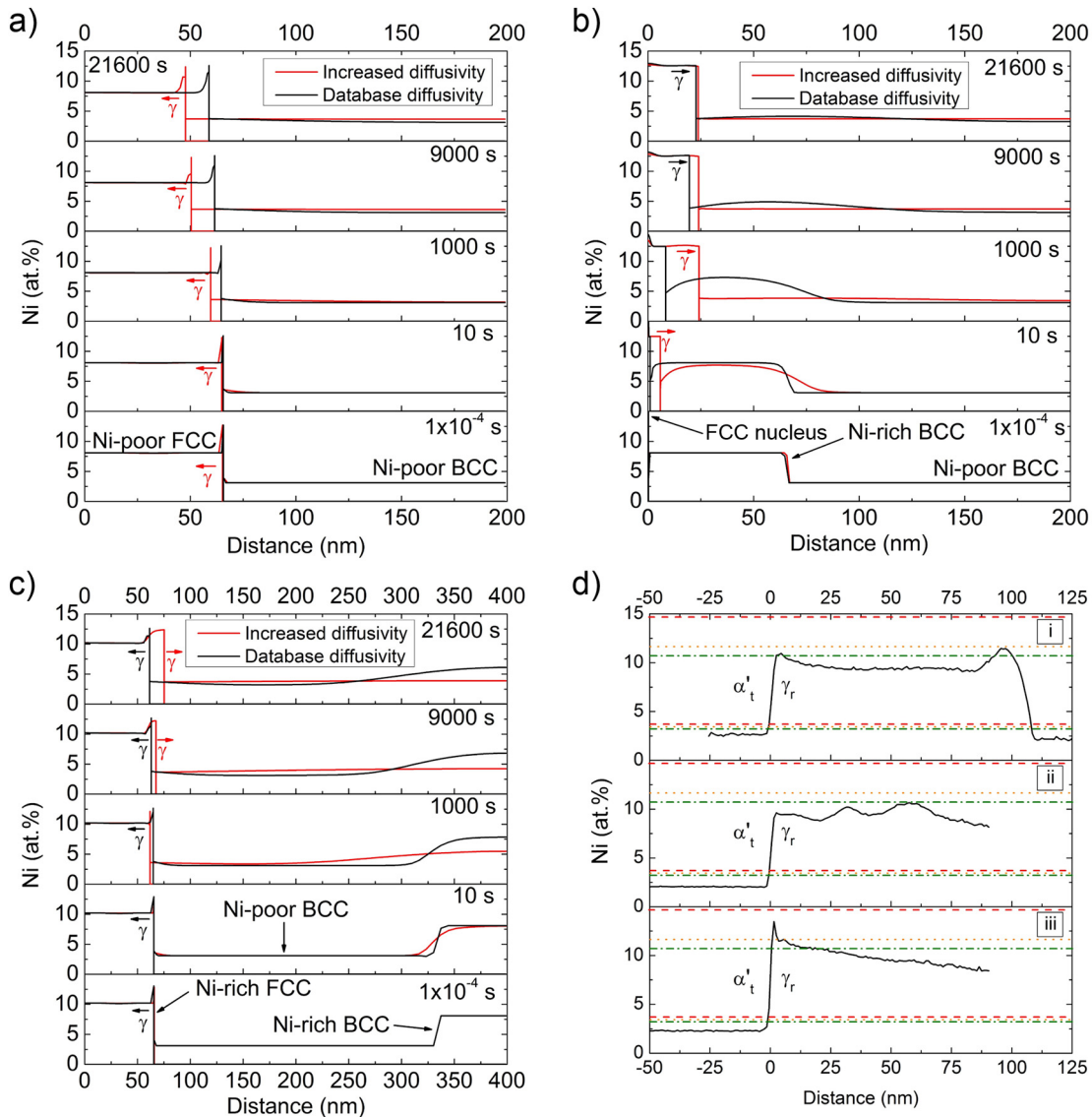


Fig. 8. Kinetic simulations of the microstructural evolution as a function of time at 600 °C, considering: a) a Ni-poor FCC lath in a Ni-poor tempered BCC matrix; b) epitaxial austenite growth of an FCC nucleus, aided by an adjacent Ni-rich BCC lath in a Ni-poor tempered BCC matrix; c) a Ni-rich FCC lath in a Ni-poor tempered BCC matrix, aided by a Ni-rich BCC lath separated by a typical lath distance; d) three experimental cases of γ_r/α'_t interfaces, measured by APT. The black and red curves in a) to c) indicate calculated profiles using database mobility and increased mobility by a factor of 50 [21], respectively. The red dashed, orange dotted and green dash-dotted lines in d) indicate the tie-line compositions expected at 580, 600 and 625 °C, respectively.

Ni concentrations between 8 and 11 wt% [10,18,24,44,48]. According to kinetic studies published elsewhere [26], reverted austenite related to equilibrium partitioning of Ni below 8 wt% (7.5 at.%) was completely unstable upon cooling to room temperature. Additionally, it has been reported that austenite retention in SMSS can be obtained upon cooling from above the A_{c3} temperature when the nominal Ni content is increased above 8 [49] and 9 wt% [50]. From our experimental data, it is expected that complete austenite stability will be reached when the Ni content inside the reverted laths is at least above 9.5 at.%, which is consistent with the literature.

On the other hand, the austenite stability upon cooling has been also related to the Hall-Petch effect due to austenite strengthening via lath size reduction. The volume fraction of martensitic transformation can be associated to the cube of the austenite grain size [51]. Low inter-critical tempering temperatures yield to both finer and Ni-richer austenite laths [10,11,41,48] with a coherent low mobility K-S orientation [52] and higher energy barrier for martensitic transformation [44]. Since little or no PAGB and reverted lath width evolution was observed, the cyclic austenite stabilization can be associated mainly to compositional effects.

4.5. Reverted austenite vs hardness

After the suppression of the fresh martensite and maximization of the stable reverted austenite through triple ICT, the average hardness value remained stable around 275 HV. Therefore, the austenite reversion is not the only factor responsible for the hardness drop after tempering. Several approaches have been attempted to reduce SMSS hardness so as to reach the suggested maximum value of 253 HV [12]. Single and multiple ICT cycles [6,9–11,14] and even alloy modifications through reduction of interstitial elements [13], or addition of stabilizing elements [15] have been reported. For example, carbon reduction between 0.03 and 0.02 wt% in a CA6NM martensitic stainless steel, in addition to extensive double tempering at 650 °C during 10 h followed by tempering at 620 °C during 20 h, resulted in average hardness values between 270 and 260 HV [13].

The softening mechanism is complex since it involves competing effects of recovery, carbon arrest and secondary precipitation of Ti (C, N) and χ . Recovery can be expected at lower inter-critical temperatures due to the fast reduction of the dislocation density of martensite upon

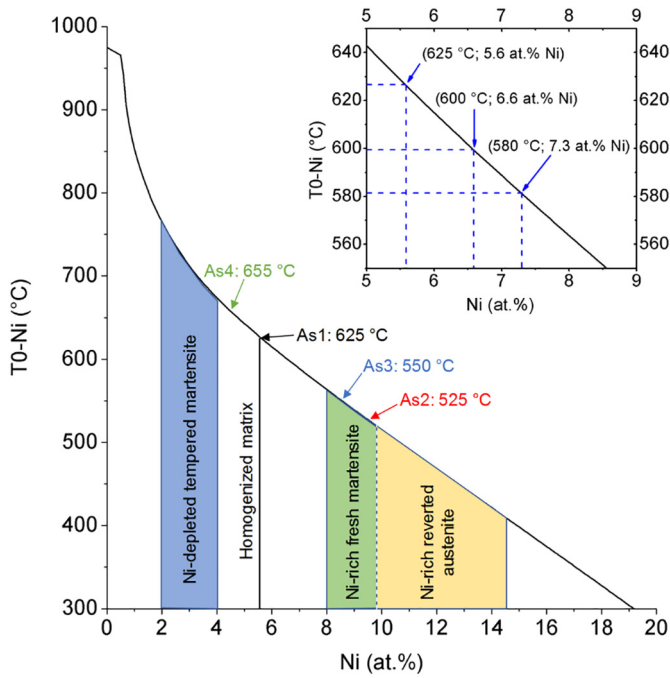


Fig. 9. Ni-zero temperature for $\alpha \leftrightarrow \gamma$ spontaneous transformation as a function of the nominal Ni content, calculated according to the SMSS nominal composition. The $\alpha'f \rightarrow \gamma$ reversion temperature (A_s) was measured during the heating stages of the first (A_{s1}), second (A_{s2}) and third (A_{s3}) ICT cycles, and during final heating (A_{s4}) to the fully austenitic field.

heating and isothermal stages, followed by little or no additional gain upon cooling [53].

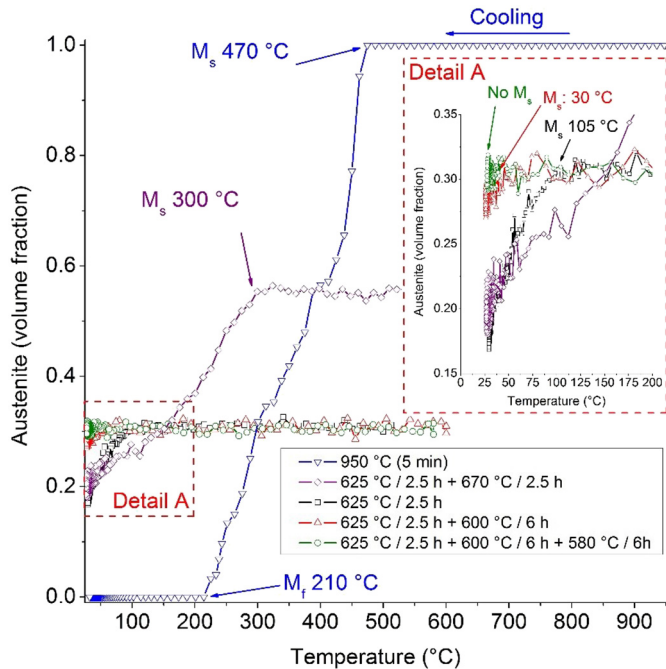


Fig. 10. Austenite to martensite transformation kinetics measured by synchrotron X-ray diffraction upon cooling from the first, second and third inter-critical tempering cycles, and from complete austenitization at 950 °C. The martensitic start transformation was measured at the surface of the sample. The red dashed square shows a detailed view of the martensitic transformation between 200 °C and room temperature. The experimental error for SXRD data ranges between 0.005 and 0.015 vol fraction.

Carbon arrest has been reported to occur in SMSS due to the precipitation of Ti (C, N) and $M_{23}C_6$ [24,41]. The carbon content in the homogenized condition, and after simple and triple ICT cycles was determined by APT through peak deconvolution analysis. As shown in Table 5, before tempering, a small concentration of carbon was present in solid solution. This is due to unfinished Ti (C, N) precipitation upon cooling from the austenitic field after the homogenization step. After single ICT at 625 °C for 2.5 h, virtually carbon-free γ_f and the α'_f were found due to the additional precipitation of Ti (C, N) [17]. After triple ICT, little or no further carbon arrest was observed. According to Sømme, the secondary hardening effect of Ti (C, N) in a Ti-stabilized SMSS was shown to be restricted only to the first 30 min of inter-critical tempering [54]. Therefore, this effect is not expected to be observable in the case presented in this investigation due to the extended multiple-step inter-critical cycles.

The effect of the precipitation of χ is more complex due to the lack of information of such precipitate in SMSS. Nevertheless, the precipitation of χ and σ in duplex stainless steels has shown to produce a secondary hardening effect. The quantification of the actual volume fractions involved in such phenomena was not completely clarified [55,56]. However, according to Wan et al., the volume fraction of σ can increase up to 0.11 after 15 h of isothermal soaking at 850 °C, respectively. Nonetheless, the secondary hardening effect was observed only for annealing times below 3 h and volume fractions of σ up to 0.015 [57]. For the case of SMSS, the equilibrium volume fraction of χ at the temperatures of interest is below 0.05 and its contribution to secondary hardening cannot be readily isolated. Therefore, a strong reduction in the dislocation density accompanied by the formation of virtually carbon-free austenite and martensite during the first ICT cycle is the main reasons for the steady hardness values observed after double and triple ICT cycles. A schematic summary of the transformation sequence throughout the multiple-step inter-critical tempering is shown in Fig. 11.

5. Conclusions

The mechanism for austenite reversion and stabilization during multiple-step inter-critical tempering of a Ti-stabilized supermartensitic stainless steel was studied using synchrotron X-ray diffraction, Scanning Transmission Electron Microscopy, Energy Dispersive X-ray Spectroscopy, Atom Probe Tomography, microhardness, thermodynamic and kinetic simulations. The main results can be summarized as follows:

- After single inter-critical tempering at 625 °C during 2.5 h, a compositionally non-homogeneous microstructure was produced due to the total reversion of 0.32 γ in high temperature. Three constituents were identified: 0.18 Ni-rich stable reverted austenite laths, 0.14 Ni-rich fresh martensite laths and 0.68 Ni-depleted tempered martensite matrix (volume fractions). Both stable and unstable laths were morphologically similar but compositionally differentiable.
- The asymptotic behavior of the isothermal reversion kinetics towards a volume fraction of 0.32 γ during double and triple ICT cycles, demonstrated the imposition of a meta-equilibrium transition microstructure granted by the first ICT cycle. In both cases, the total volume fraction of reverted austenite of 0.32 was above the global equilibrium of 0.24 γ and 0.18 γ , expected at 600 and 580 °C, respectively.
- The mechanism behind the progressive increase in stable reverted austenite at room temperature after double and triple ICT cycles, with a limit of 0.32 γ , was associated to two main factors: the Ni-rich α'_f laths acting as local Ni containers, providing site-specific reversion of austenite; and the suppression of any additional nucleation at the Ni-poor matrix as the T0 temperature for austenite reversion was strongly increased.

Table 5
ROI compositional analysis performed by APT of the fresh martensite (before tempering), and the reverted austenite and tempered martensite (after single and triple ICT). IVAS peak deconvolution analysis.

Element	Homogenized		1 ICT				3 ICT			
	Fresh martensite		Tempered martensite		Reverted austenite		Tempered martensite		Reverted austenite	
	at.%	% error	at.%	% error	at.%	% error	at.%	% error	at.%	% error
Fe	79.172	0.053	81.713	0.014	74.335	0.015	83.158	0.038	74.264	0.04
Cr	12.824	0.009	12.703	0.012	12.746	0.012	12.567	0.036	13.147	0.03
Ni	5.486	0.005	3.110	0.007	10.195	0.007	2.105	0.014	9.833	0.02
Mo	1.095	0.002	1.196	0.003	0.96	0.003	1.114	0.008	1.042	0.01
Ti	0.084	0.001	0.042	0.001	0.139	0.001	0.02	0.002	0.041	0.00
C	0.023	0.001	0.001	0.000	0.000	0.000	0.0005	0.0001	0.00	0.000
Other	Bal.		Bal.		Bal.		Bal.		Bal.	

- Inhomogeneous Ni distribution along the reverted austenite laths was associated to lack of homogenization due to several factors, such as the coalescence along the lath length direction, to the low diffusivity of Ni in FCC at the double and triple ICT temperatures, the restricted lath/matrix interface mobility and to the Ni build-up at the interfaces according to the local equilibrium conditions of the reversion temperature.
- The hardness reduction observed after the single ICT cycle was associated mainly to the carbon arrest effect provided by the precipitation of Ti (C, N). Even after almost doubling the austenite volume fraction and eliminating all fresh martensite through triple ICT, no further softening was observed. This was explained by the production of virtually carbon-free austenite and tempered martensite after the first ICT cycle.

Authors contribution

All authors contributed extensively to the discussion and execution of the present work. J.D. Escobar performed the in situ synchrotron x-ray diffraction experiments, participated in the TEM, APT and CALPHAD data analysis and wrote the manuscript. J.P. Oliveira and C.A.F. Salvador conducted the FIB sample preparation and undertook the STEM microstructural characterization. G.A. Faria and J. Rodriguez conducted CALPHAD and DICTRA calculations. J.D. Poplawsky carried out and analyzed the APT experiments and performed the FIB sample preparation. P.R. Mei, S.S. Babu and A. J. Ramirez provided advice and support during the experimental design and interpretation of results. All authors revised and commented on the manuscript.

Acknowledgments

The authors acknowledge the XTMS beamline members, the Brazilian Synchrotron Light Source (LNLS) and the Metals Characterization and Processing group (CPM) at the Brazilian Nanotechnology National Laboratory (LNNano) for the support with the diffraction experiments; Villares Metals S.A. for the donation of the materials; and CNPq-SWE

Data availability

The processed data required to reproduce these findings are available to download from <https://data.mendeley.com/datasets/xn9kff8dw3/draft?a=5a5d6b8d-9359-413d-ac4c-687d0228ace0>.

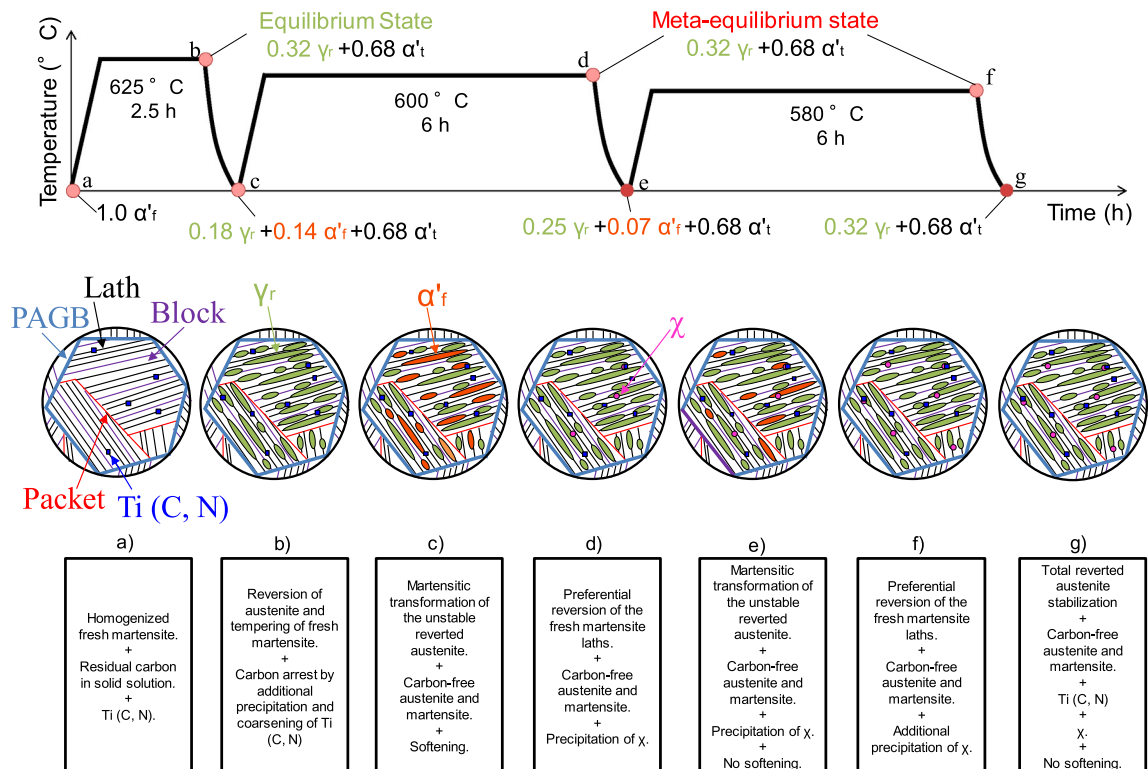


Fig. 11. Schematic representation of the transformation sequence throughout a triple inter-critical tempering of a Ti-stabilized supermartensitic stainless steel.

02766/2014-4, FAPESP (2014/20844-1), FAPESP (2016/13466-6) for the PhD funding. APT was conducted at ORNL's Center for Nanophase Materials Sciences (CNMS), which is a U.S. DOE Office of Science User Facility.

References

- [1] L. Yuan, D. Ponge, J. Wittig, P. Choi, J.A. Jiménez, D. Raabe, Nanoscale austenite reversion through partitioning, segregation and kinetic freezing: example of a ductile 2GPa Fe-Cr-C steel, *Acta Mater.* 60 (2012) 2790–2804.
- [2] M. Belde, H. Springer, D. Raabe, Vessel microstructure design: a new approach for site-specific core-shell micromechanical tailoring of TRIP-assisted ultra-high strength steels, *Acta Mater.* 112 (2016) 19–31.
- [3] M. Kuzmina, D. Ponge, D. Raabe, Grain boundary segregation engineering and austenite reversion turn embrittlement into toughness: example of a 9 wt.% medium Mn steel, *Acta Mater.* 86 (2015) 182–192.
- [4] D. Raabe, S. Sandlöbes, J. Millán, D. Ponge, H. Assadi, M. Herbig, P.P. Choi, Segregation engineering enables nanoscale martensite to austenite phase transformation at grain boundaries: a pathway to ductile martensite, *Acta Mater.* 61 (2013) 6132–6152.
- [5] D. Xu, Y. Liu, Z. Ma, H. Li, Z. Yan, Structural refinement of 00Cr13Ni5Mo2 supermartensitic stainless steel during single-stage intercritical tempering, *Int. J. Miner. Metall. Mater.* 21 (2014) 279–288.
- [6] G.F. Silva, S.S.M. Tavares, J.M. Pardal, M.R. Silva, H.F.G. Abreu, Influence of heat treatments on toughness and sensitization of a Ti-alloyed supermartensitic stainless steel, *J. Mater. Sci.* 46 (2011) 7737–7744.
- [7] D. Zou, Y. Han, W. Zhang, X. Fang, Influence of tempering process on mechanical properties of 00Cr13Ni4Mo supermartensitic stainless steel, *J. Iron Steel Res. Int.* 17 (2010) 50–54.
- [8] Y. Liu, Y. Dong, Q.L. Yong, J. Su, K.Y. Zhao, W. Jiang, Effect of heat treatment on microstructure and property of Cr13 supermartensitic stainless steel, *J. Iron Steel Res. Int.* 18 (2011) 60–66.
- [9] X.P. Ma, L.J. Wang, C.M. Liu, S.V. Subramanian, Microstructure and properties of 13Cr5Ni1Mo0.025Nb0.09V0.06N supermartensitic stainless steel, *Mater. Sci. Eng. A* 539 (2012) 271–279.
- [10] P.D. Bilmes, M. Solari, C.L. Llorente, Characteristics and effects of austenite resulting from tempering of 13Cr-NiMo martensitic steel weld metals, *Mater. Charact.* 46 (2001) 285–296.
- [11] W.-H. Yuan, X.-H. Gng, Y.-Q. Sun, J.-X. Liang, Microstructure evolution and precipitation behavior of 0Cr16Ni5Mo martensitic stainless steel during tempering process, *J. Iron Steel Res. Int.* 23 (2016) 401–408.
- [12] NACE International, ANSI/NACE MR0175/ISO 15156: Petroleum and Natural Gas Industries, Materials for Use in H2S Containing Environments in Oil and Gas Production, 2002 (Houston).
- [13] T.G. Gooch, Heat Treatment of Welded 13Cr-4%Ni Martensitic Stainless Steels for Sour Service, *Welding Research Supplement*, 1995 214–223.
- [14] S.S.M. Tavares, C.R. Rodrigues, J.M. Pardal, E.S. Barbosa, H.F.G. Abreu, Effect of post weld heat treatments on the microstructure and mechanical properties of dissimilar weld of supermartensitic stainless steel, *Mater. Res.* 17 (2014) 1336–1343.
- [15] C.A.D. Rodrigues, P.L.D. Lorenzo, A. Sokolowski, C.A. Barbosa, J.M.D.A. Rollo, Titanium and molybdenum content in supermartensitic stainless steel, *Mater. Sci. Eng. A* 460–461 (2007) 149–152.
- [16] A. Bojack, L. Zhao, P.F. Morris, J. Sietsma, In situ thermo-magnetic investigation of the austenitic phase during tempering of a 13Cr6Ni2Mo supermartensitic stainless steel, *Metall. Mater. Trans. A* 45 (2014) 5956–5967.
- [17] J.D. Escobar, J.D. Poplawsky, G.A. Faria, J. Rodriguez, J.P. Oliveira, C.A.F. Salvador, P.R. Mei, S.S. Babu, A.J. Ramirez, Compositional analysis on the reverted austenite and tempered martensite in a Ti-stabilized supermartensitic stainless steel: segregation, partitioning and carbide precipitation, *Mater. Des.* 140 (2018) 95–105.
- [18] Y.K. Lee, H. Shin, D. Leem, J. Choi, W. Jin, C. Choi, Reverse transformation mechanism of martensite to austenite and amount of retained austenite after reverse transformation in Fe-3Si-13Cr-7Ni (wt-%) martensitic stainless steel, *Mater. Sci. Technol.* 19 (2003) 393–398.
- [19] D. Leem, Y. Lee, J. Jun, C. Choi, Amount of retained austenite at room temperature after reverse transformation of martensite to austenite in an Fe-13Cr-7Ni-3Si martensitic stainless steel, *Scr. Mater.* 45 (2001) 767–772.
- [20] M. Karlsen, Ø. Grong, M. Sofferud, J. Hjelen, G. Rørvik, R. Chiron, Scanning electron microscopy/electron backscatter diffraction based observations of martensite variant selection and slip plane activity in supermartensitic stainless steels during plastic deformation at elevated, ambient, and subzero temperatures, *Metall. Mater. Trans. A* 40 (2009) 310–320.
- [21] O. Dmitrieva, D. Ponge, G. Inden, J. Millán, P. Choi, J. Sietsma, D. Raabe, Chemical gradients across phase boundaries between martensite and austenite in steel studied by atom probe tomography and simulation, *Acta Mater.* 59 (2011) 364–374.
- [22] A. Bojack, L. Zhao, P.F. Morris, J. Sietsma, In-situ determination of austenite and martensite formation in 13Cr6Ni2Mo supermartensitic stainless steel, *Mater. Charact.* 71 (2012) 77–86.
- [23] A. Bojack, L. Zhao, P.F. Morris, J. Sietsma, Austenite formation from martensite in a 13Cr6Ni2Mo supermartensitic stainless steel, *Metall. Mater. Trans. A* 47A (2016) 1996–2009.
- [24] Y.Y. Song, D.H. Ping, F.X. Yin, X.Y. Li, Y.Y. Li, Microstructural evolution and low temperature impact toughness of a Fe-13Cr-4%Ni-Mo martensitic stainless steel, *Mater. Sci. Eng. A* 527 (2010) 614–618.
- [25] M. Belde, H. Springer, G. Inden, D. Raabe, Multiphase microstructures via confined precipitation and dissolution of vessel phases: example of austenite in martensitic steel, *Acta Mater.* 86 (2015) 1–14.
- [26] J.D. Escobar, G.A. Faria, L. Wu, J.P. Oliveira, P.R. Mei, A.J. Ramirez, Austenite reversion kinetics and stability during tempering of a Ti-stabilized supermartensitic stainless steel: correlative in situ synchrotron X-ray diffraction and dilatometry, *Acta Mater.* 138 (2017) 92–99.
- [27] G.A. Faria, Exploring Metallic Materials Behavior Through In Situ Crystallographic Studies, State University of Campinas, 2014.
- [28] M.K. Miller, Atom Probe Tomography: Analysis at the Atomic Level, Springer US, 2000.
- [29] M. Kuzmina, M. Herbig, D. Ponge, S. Sandlöbes, D. Raabe, Linear complexions: confined chemical and structural states at dislocations, *Science* 349 (2015) 1080–1083.
- [30] J. Pak, D.W. Suh, H.K.D.H. Bhadeshia, Displacive phase transformation and surface effects associated with confocal laser scanning microscopy, *Metall. Mater. Trans. A* 43 (2012) 4520–4525.
- [31] M. Karlsen, J. Hjelen, Ø. Grong, G. Rørvik, R. Chiron, U. Schubert, E. Nilsen, SEM/EBSD based in situ studies of deformation induced phase transformations in supermartensitic stainless steels, *Mater. Sci. Technol.* 24 (2008) 64–72.
- [32] J. Han, A.K. da Silva, D. Ponge, D. Raabe, S.-M. Lee, Y.-K. Lee, S.-I. Lee, B. Hwang, The effects of prior austenite grain boundaries and microstructural morphology on the impact toughness of intercritically annealed medium Mn steel, *Acta Mater.* 122 (2017) 199–206.
- [33] J. Dong, C. Liu, Y. Liu, C. Li, Q. Guo, H. Li, Effects of two different types of MX carbonitrides on austenite growth behavior of NbVTi micro alloyed ultra-high strength steel, *Fusion Eng. Des.* (2017) 415–422.
- [34] S. Morito, H. Tanaka, R. Konishi, T. Furuhashi, T. Maki, The morphology and crystallography of lath martensite in Fe-C alloys, *Acta Mater.* 51 (2003) 1789–1799.
- [35] M.-M. Wang, C.C. Tasan, D. Ponge, A.-Ch. Dippel, D. Raabe, Nanolaminate transformation-induced plasticity-twinning-induced plasticity steel with dynamic strain partitioning and enhanced damage resistance, *Acta Mater.* 85 (2015) 216–228.
- [36] F.G. Caballero, M.K. Miller, S.S. Babu, C. Garcia-Mateo, Atomic scale observations of bainite transformation in a high carbon high silicon steel, *Acta Mater.* 55 (2007) 381–390.
- [37] F.G. Caballero, M.K. Miller, C. Garcia-Mateo, Carbon supersaturation of ferrite in a nanocrystalline bainitic steel, *Acta Mater.* 58 (2010) 2338–2343.
- [38] E.V. Pereloma, I.B. Timokhina, M.K. Miller, P.D. Hodgson, Three-dimensional atom probe analysis of solute distribution in thermomechanically processed TRIP steels, *Acta Mater.* 55 (2007) 2587–2598.
- [39] M. Peet, S.S. Babu, M.K. Miller, H.K.D.H. Bhadeshia, Three-dimensional atom probe analysis of carbon distribution in low-temperature bainite, *Scr. Mater.* 50 (2004) 1277–1281.
- [40] F. Niessen, M. Villa, J. Hald, M.A.J. Somers, Kinetics analysis of two-stage austenitization in supermartensitic stainless steel, *Mater. Des.* 116 (2017) 8–15.
- [41] F. Niessen, Austenite reversion in low-carbon martensitic stainless steel – a CALPHAD-assisted review, *Mater. Sci. Technol.* (2018) 1–14.
- [42] L. Morsdorf, C.C. Tasan, D. Ponge, D. Raabe, 3D structural and atomic-scale analysis of lath martensite: effect of the transformation sequence, *Acta Mater.* 95 (2015) 366–377.
- [43] S.H. Mun, M. Watanabe, X. Li, K.H. Oh, D.B. Williams, H.C. Lee, Precipitation of austenite particles at grain boundaries during aging of Fe-Mn-Ni steel, *Metall. Mater. Trans. A* 33 (2002) 1057–1067.
- [44] S. Zhang, P. Wang, D. Li, Y. Li, Investigation of the evolution of retained austenite in Fe-13Cr-4%Ni martensitic stainless steel during intercritical tempering, *Mater. Des.* 84 (2015) 385–394.
- [45] R. Schnitzer, R. Raids, M. Nöhrer, M. Schober, R. Hochfellner, S. Zinner, E. Poveden-Karadeniz, E. Kozeschnik, H. Leitner, Reverted austenite in PH 13-8 Mo maraging steels, *Mater. Chem. Phys.* 122 (2010) 138–145.
- [46] S. Nag, R. Banerjee, R. Srinivasan, J.Y. Hwang, M. Harper, H.L. Fraser, ω -Assisted nucleation and growth of α precipitates in the Ti-5Al-5Mo-5V-3Cr-0.5Fe β titanium alloy, *Acta Mater.* 57 (2009) 2136–2147.
- [47] A. Bojack, L. Zhao, J. Sietsma, Thermodynamic analysis of the effect of compositional inhomogeneity on phase transformations in a 13Cr6Ni2Mo supermartensitic stainless steel, *Solid State Phenom.* 172–174 (2011) 899–904.
- [48] K. Kondo, H. Amaya, T. Ohmura, K. Moriguchi, Effect of cold work on retained austenite and on corrosion performance in low carbon martensitic stainless steels, *Corrosion 2003*, NACE International, Houston, Texas, 2003, (Paper 0394).
- [49] S. Zhang, H. Terazaki, Y. Komizo, In-situ observation of martensite transformation and retained austenite in supermartensitic stainless steel, *Trans. JWRI* 39 (2012) 115–117.
- [50] K. Kondo, M. Ueda, K. Ogawa, H. Amaya, H. Hirata, H. Takabe, Alloy design of super 13 Cr martensitic stainless steel (development of super 13 Cr martensitic stainless steel for line pipe), *Supermartensitic Stainless Steels '99*, Belgium 1999, pp. 11–18.
- [51] H. Yanga, H.K.D.H. Bhadeshia, Austenite grain size and the martensite-start temperature, *Scr. Mater.* 60 (2009) 493–495.
- [52] L. Liu, Z.G. Yang, C. Zhang, W.B. Liu, An in situ study on austenite memory and austenitic spontaneous recrystallization of a martensitic steel, *Mater. Sci. Eng. A* 527 (2010) 7204–7209.
- [53] M. Wiessner, E. Gamsjäger, S. van der Zwaag, P. Angerer, Effect of reverted austenite on tensile and impact strength in a martensitic stainless steel – an in-situ X-ray diffraction study, *Mater. Sci. Eng. A* 682 (2017) 117–125.
- [54] A. Sømme, Secondary Hardening in Two Supermartensitic Stainless Steels, Norwegian University of Science and Technology, 2012.
- [55] S.K. Ghosh, S. Mondal, High temperature ageing behavior of a duplex stainless steel, *Mater. Charact.* 12 (2008) 1776–1783.
- [56] Y.Q. Wang, J. Han, H.C. Wu, B. Yang, X.T. Wang, Effect of sigma phase precipitation on the mechanical and wear properties of Z3CN20.09M cast duplex stainless steel, *Nucl. Eng. Des.* 259 (2013) 1–7.
- [57] J. Wan, H. Ruan, J. Wang, S. Shi, The kinetic diagram of sigma phase and its precipitation hardening on 15Cr-2Ni duplex stainless steel, *Mater. Sci. Eng. A* 711 (2018) 571–578.